https://doi.org/10.5194/egusphere-2026-5514
Preprint. Discussion started: 17 September 2026

Intra-tidal bed evolution on a macrotidal dissipative beach during a storm: contrasting roles of extremely shallow and relatively deep water stages

Zheyu Xiao[1], Feng Cai[2], Hongshuai Qi[2], Benwei Shi[3], Shaohua Zhao[2], Gen Liu[2], Yanyu He[2], Chao Cao[2], Chengtao Wang[4], Hang Yin[5], Bipeng Hui[5]

[1] College of Marine Living Resource Sciences and Management, Shanghai Ocean University, 200100, China,
[2] Third Institute of Oceanography, Ministry of Natural Resources, 361001, China
[3] State Key Laboratory of Estuarine and Coastal Research, East China Normal University, 200000, China
[4] College of Marine Science and Technology, China University of Geosciences, 430000, China
[5] College of Ocean and Earth Sciences, Xiamen University, Xiamen, 361104, China

Correspondence to: Feng Cai (fcai800@126.com)

Abstract. Intra-tidal morphodynamics on macrotidal dissipative beaches remain poorly understood due to challenges in capturing continuous bed-level evolution under shallow-water conditions. Here, we used a high-resolution vertical probe (Argus Surface Meter, ASM) to obtain minute-scale, continuous records of bed elevation and near-bed suspended sediment concentration (SSC) in the intertidal zone across Extremely Shallow Water Stages (ESWS, water depths < 0.3 m) and Relatively Deep Water Stages (RDWS, water depths > 0.3 m) during storm attenuation. Our results reveal three key findings: (1) The relative dominance of ESWS and RDWS in bed-level evolution reverses as storm decays. RDWS drives the most significant changes under storm conditions, while the contribution of ESWS increases substantially as storm decays, becoming predominant in fair weather when bed shear stress falls below the critical threshold in RDWS. (2) A consistent flood-phase erosion–ebb-phase accretion pattern characterizes ESWS, whereas RDWS exhibits state-dependent behavior: under storms, this pattern is maintained by tide-modulated sediment supply—with active scouring during flood due to high transport capacity and deposition during ebb due to overwhelming sediment delivery from the migrating breaker zone. In fair weather, it reverses to flood-accretion/ebb-erosion due to settling of sediment during flood and subsequent resuspension during ebb. (3) the interplay between ESWS and RDWS highlights the critical role of complete ESWS process in sustaining dissipative beach stability. Based on these findings, we propose a conceptual model integrating ESWS and RDWS, providing a basis for predicting intertidal morphodynamic evolution in tide-dominated systems under changing storms.

1 Introduction

Beach morphodynamics are governed by complex feedbacks between sediment transport and hydrodynamic forcing(Anthony and Aagaard, 2020; Masselink and Puleo, 2006), particularly in the intertidal zone. As sea levels rise and storm intensity

https://doi.org/10.5194/egusphere-2026-5514
Preprint. Discussion started: 17 September 2026

increases, a mechanistic understanding of these processes becomes critical for enhancing coastal resilience. Beaches are commonly classified into reflective, dissipative, and intermediate types based on their profile morphology, each exhibiting distinct evolutionary patterns(Aagaard et al., 2013). Among these, dissipative beaches tend to show greater morphological stability during storms due to their low-gradient profiles (Aagaard et al., 2013; Qi et al., 2010; Rangel-Buitrago and Anfuso, 2011; Wright and Short, 1984). These gentle slopes prolong the duration of shallow water process, thereby intensifying nonlinear interactions between wave breaking, bed friction, and sediment resuspension(António et al., 2023; Grasso et al., 2009). Therefore, investigating the morphodynamics during shallow water is essential for deciphering the underlying mechanisms of dissipative beach evolution during extreme events.

Although previous studies have advanced our understanding of shallow water processes, much of this work has focused on independent or weakly coupled swash and surf processes(Aagaard et al., 2018; Blenkinsopp et al., 2011; Puleo, 2009; Puleo et al., 2014). As a result, continuous models capable of capturing morphological evolution from swash to surf remain limited, and this leaves a key knowledge gap: an insufficient understanding of continuous hydrodynamic–sediment–morphological processes across the tidal cycle—particularly regarding the contrasting roles of Extremely Shallow Water Stages (ESWS, defined as water depths $h< 0.3$ m) and Relatively Deep Water Stages (RDWS, defined as water depths $h > 0.3$ m). These stages likely govern beach stability through distinct sediment contributions, yet still poorly quantified.

ESWS has garnered increasing attention in tidal flat research, where its short-duration, high-intensity hydrodynamic forcing drives disproportionate sediment flux and morphological change(Shi et al., 2017, 2019; Zhang et al., 2016). Dissipative beaches exhibit even more pronounced ESWS effects due to their wide intertidal zones—similar to those in tidal flats—compared to reflective or intermediate beaches. In dissipative beaches, infiltration during uprush generally attenuates backwash strength, promoting net onshore transport, whereas exfiltration during falling tide enhances offshore-directed flows (Puleo et al., 2014; Turner and Masselink, 1998). These unique hydrodynamic characteristics allow ESWS and RDWS to influence sediment connectivity across the intertidal zone, requiring a beach-scale holistic perspective instead of isolated analysis of swash or surf processes.

Despite its importance, continuous monitoring of bed-level evolution across tidal cycles remains a challenge due to the periodic transition between subaerial exposure and submergence(Brand et al., 2020). These dynamic conditions require instrumentation capable of seamless operation across the air–water interface, while preserving measurement accuracy in the presence of aerated, high-energy storm waves—capabilities that conventional acoustic sensors typically lack (Hu et al., 2023; Masselink et al., 2007; van der Werf et al., 2022). As a result, high-resolution, continuous measurements that simultaneously capture bed elevation and sediment dynamics across the full tidal range are exceptionally rare.

To address this limitation, we deployed an Argus Surface Meter (ASM), a vertical probe equipped with 96 optical sensors, to achieve high-resolution bed-level fluctuations and near-bed sediment concentrations. Over four days on a macrotidal dissipative beach in the Taiwan Strait, we collected synchronized data across eight tidal cycles in the intertidal zone under both typhoon-induced and calm wave conditions. Our objectives were to:(1) characterize bed-level responses to varying hydrodynamic regimes, (2) quantify the morphological contribution of ESWS relative to RDWS, and (3) identify how tidal

https://doi.org/10.5194/egusphere-2026-5514
Preprint. Discussion started: 17 September 2026

modulation controls sediment availability and transport. Finally, we propose a conceptual model integrating these processes to explain the observed morphodynamic behavior of dissipative beaches during extreme events.

2 Field site

The study area is located at Yuandangao Beach (YDA) in the southern part of Pingtan Island, Fujian Province, China (Fig.1a). The beach is located on the western side of the Taiwan Strait and characterized by a regular semi-diurnal tidal regime, with a mean spring tide range of 5.4 m and a maximum range of up to 6.7 m. YDA is a cape-bay beach approximately 1.5 km long and oriented roughly north-south, with headlands bounding both ends (Fig.1b, c). The beach is dissipative, featuring a gently sloping (~ 0.02) intertidal zone approximately 300-400 m wide. In the central intertidal zone, a continuous shore-parallel sand ridge is present (He et al., 2022), relic sand ripples are evident in the upper intertidal zone, while the bed is flat near the mean low water level. The median grain size at the study site was approximately 0.19 mm. Due to abundant sediment supply and prevailing onshore winds, the beach-dune system in the study area is well-developed, with the backshore dunes reaching heights of 4-7 m.

Influenced by the narrow channel effect of the Taiwan Strait, the hydrodynamics at YDA are characterized by weak winds and low waves during the summer ($H_S < 0.3m$), and strong winds and high waves during the winter. From October to May, northeast winds prevail, with an average wind speed of approximately 11 m s^{-1} and about 70% of wave heights exceeding 1.5 m. In contrast, from June to August, southwest winds dominate, with an average wind speed of around 6 m s^{-1}, primarily generating waves below 1.5 m. The study area is frequently affected by tropical storms during summer. Typhoon Doksuri, with super typhoon intensity, entered the South China Sea on July 27, 2023. It then entered the Taiwan Strait on July 28 and made landfall at 09:00 on the same day, approximately 145 km southwest of the study area, with landfall winds reaching speeds of over 50 m s^{-1}, subjecting YDA to a storm wave event (Fig 1a).

https://doi.org/10.5194/egusphere-2026-5514
Preprint. Discussion started: 17 September 2026

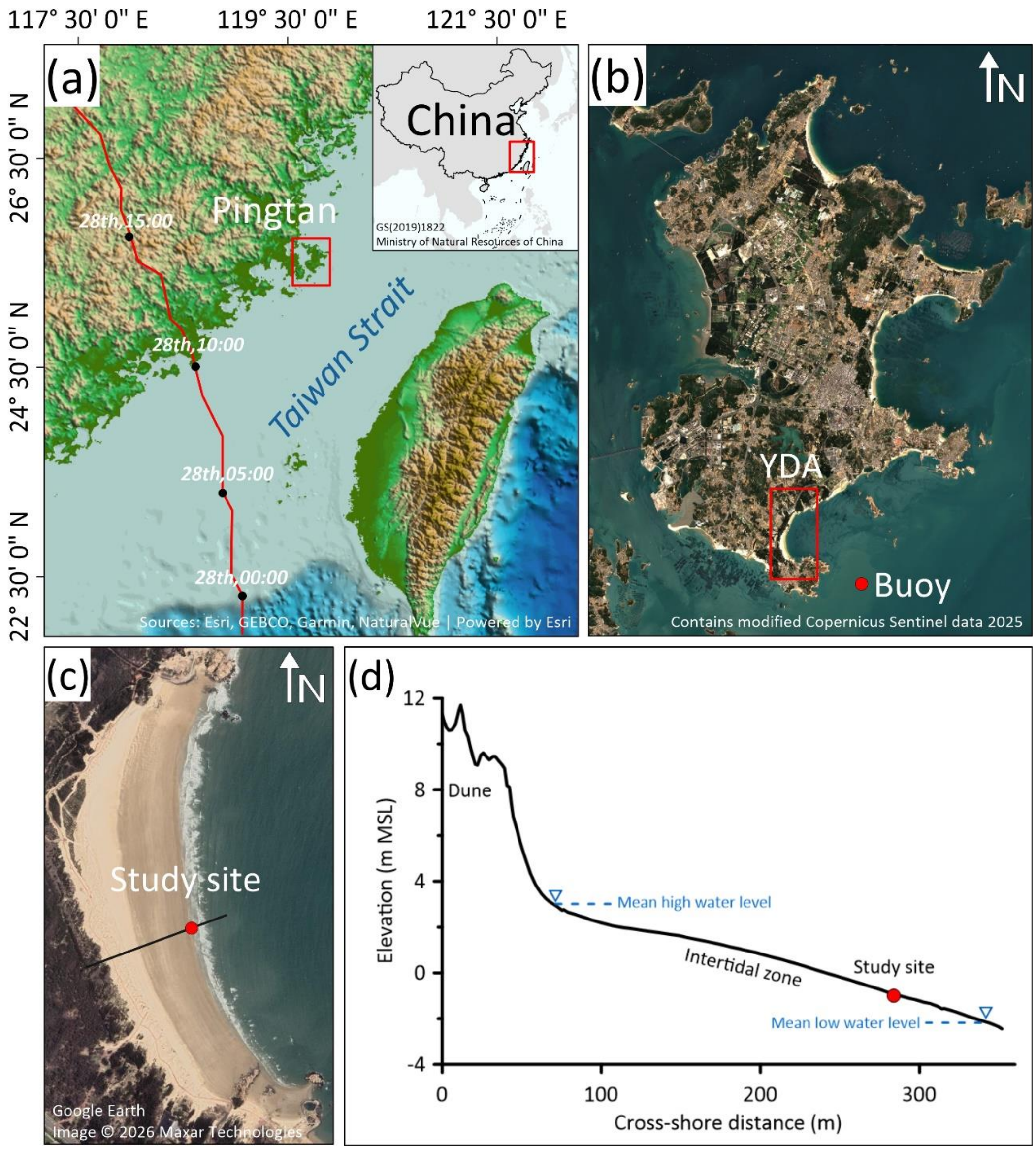

Figure 1: Regional setting and field-site configuration. (a) Track of Typhoon Doksuri. (b) Pingtan Island and Yuandangao Beach (YDA) and the offshore wave buoy. (c) Plan view of YDA. (d) Cross-shore beach profile.

3 Materials and methods

3.1 Field measurements

In situ hydrodynamic, bed-level, and sediment conditions were measured in the lower intertidal zone at YDA from 27 to 31 July 2023. (Fig. 1d). A stainless-steel frame was deployed to support an Acoustic Doppler Current Profiler (ADCP, Nortek

https://doi.org/10.5194/egusphere-2026-5514
Preprint. Discussion started: 17 September 2026

Group, Rud, Norway), an RBRsolo3 Pressure Transducer (RBR Ltd., Ottawa, Canada), and an Argus Surface Meter (ASM IV, ARGUS Gesellschaft für Umweltmeßtechnik, Ritterhude, Germany).

The ADCP was installed downward-facing at 80 cm above the seabed to capture mean current velocity profiles at a 1-minute interval (Table 1; Fig. 2a). The RBR was positioned 30 cm above the bed, sampling at 4 Hz to record wave and water-level time series. Simultaneously, the ASM utilized a vertical array of 96 optical backscatter sensors (1-cm spacing) to record turbidity and bed-level evolution at 1 minute interval. To ensure data integrity, the internal clocks of all instruments were synchronized, and the structural stability of the frame was verified through tilt records and height verifications before and after deployment. As the instruments were deployed above the mean low water level (Fig. 1d), only the ASM continued to record data during the ESWS, while no data were recorded by the other instruments upon exposure to air.

The bed-level detection principle of the ASM is based on the differential infrared reflectance values between air, water, and bed. Due to the significantly higher reflectivity of bed sediments compared to water or air, the seabed interface can be precisely located by capturing the gradient in reflection intensity (Fig. 2b). When sensors are fully buried, the signals exhibit high reflectance and low variance, allowing high-resolution monitoring of erosion and deposition processes. While the ASM is predominantly applied to characterize bottom boundary layer dynamics (Liu et al., 2022; Niu et al., 2023), it nonetheless exhibits a reliable capacity for resolving the fluid–bed interface. The instrument's efficacy for bed-level monitoring has been substantiated in specialized field technical reports and investigations (e.g., Gilpin, 2003; Liu et al., 2021; Wen et al., 2020). Furthermore, similar vertical-array instruments designed to capture small-scale coastal morphodynamics have also been extensively validated in intertidal research (Fan et al., 2023; Hu et al., 2015; Puleo et al., 2014).

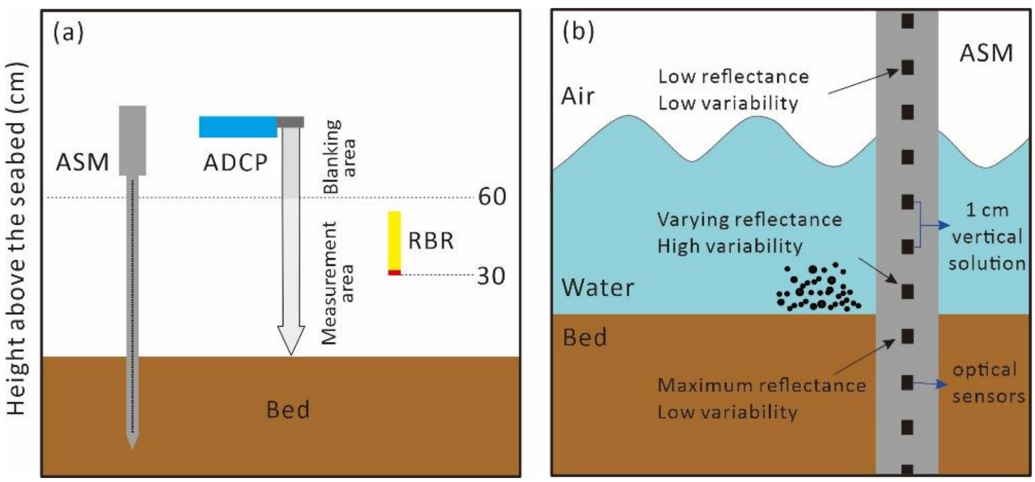

Figure 2: Instrumentation and ASM measurement principle. (a) Instrument configuration at the study site. (b) Schematic of the ASM bed-level measurement principle.

Table 1: Sampling Parameters and Deployment Heights of Instruments

Instrument	Sampling frequency (burst interval)	Height above bed (cm)	Measured parameters
RBR	4 Hz (5min)	30	Water depth, wave height and period

https://doi.org/10.5194/egusphere-2026-5514
Preprint. Discussion started: 17 September 2026

ADCP	1/60 Hz (continuous)	80	Current velocity profile
ASM IV	1/60 Hz (continuous)	-15*	Turbidity, bed-level

*The ASM IV was inserted into the seabed.

3.2 Data processing

3.2.1 Classification of ESWS and RDWS

To evaluate the morphodynamic responses across different water levels, each tidal cycle was categorized into two submerged stages: ESWS and RDWS. The transition between these stages was defined by a water depth (h) threshold of 0.3 m, representing the minimum immersion depth required for the RBR. RDWS encompasses periods where $h > 0.3m$, specifically the duration between high tide peak and the 0.3 m depth. Conversely, ESWS represents the remaining submerged duration between the 0.3 m depth and the point of complete subaerial exposure. The transition between ESWS and subaerial exposure was identified using ASM signal features: during ebb tides, the termination of ESWS was marked by the transition from a water–bed interface (high variability) to an air–bed interface (low variability), whereas the reverse process marked the onset of flood process (Fig. 2b).

To quantify the morphological evolution, Net bed-level change (NBLC) and Gross bed-level change (GBLC) of each stage were estimated as follows:

$$NBLC = z(t_{end}) - z(t_{start}) \tag{1}$$

$$GBLC = \sum_{i=1}^{n} |z(t_{i+1}) - z(t_i)| \tag{2}$$

Where $z(t_{start})$and $z(t_{end})$ are the bed levels at the start and end of each stage, and $z(t_i)$ is the bed level at time t.

3.2.2 Bed shear stress

To evaluate extreme dynamics during the typhoon, the total shear stress from combined wave and current (τ_{cw})was calculated as follows (Grant and Madsen, 1979):

$$\tau_{cw} = \sqrt{(\tau_w + \tau_c|cos\varphi|)^2 + (\tau_c|sin\varphi|)^2} \tag{3}$$

Where φ is the angle between the wave and current direction. The resulting upper-bound τ_{cw} was compared with the critical bed shear stress τ_{cr} as follows to determine the intensity of sediment motion(Soulsby, 1997):

$$\tau_{cr} = \theta_{cr}(\rho_s - \rho_w)gD_{50} \tag{4}$$

$$\theta_{cr} = \frac{0.3}{(1 + 1.2D^*)} + 0.055\big(1 - exp(-0.02D^*)\big) \tag{5}$$

https://doi.org/10.5194/egusphere-2026-5514
Preprint. Discussion started: 17 September 2026

$$D^* = \left(\frac{g(s-1)}{\nu^2}\right)^{1/3} D_{50} \tag{6}$$

Where θ_{cr} is threshold Shields parameter, D^* is the dimensionless grain size, ρ_s is the density of sediments (2650 kg/m^3), ν is the kinematic viscosity of water.

The bed shear stress was computed separately for waves (subscript w) and currents (subscript c),

$$\tau_c = \rho u_{*c}^2 \tag{7}$$

$$\tau_w = 0.5\rho_w f_w U_b^2 \tag{8}$$

with $u_{*c} = \kappa u(z)/ln(z/z_0)$, and $f_w = exp(5.213(k_s/A)^{0.194} - 5.977)$(Swart, 1974), where ρ_w is the density of water; U_b is the orbital velocity of the waves on the bottom; z is the height of the first layer above the bottom; $u(z)$ is the associated speed; κ is the Von Kármán constant (0.4); and A is the orbital half-excursion near the bottom(Soulsby, 1997), where $A = U_b T/2\pi$. The physical roughness length, k_s is defined as $k_s = 2.5D_{50}$ (Nielsen, 1992).

3.2.3 Suspended sediment concentration and Continuous bed-level

The vertical OBS sensors of ASM measure turbidity by recording light backscatter from solid particles in the multiphase flow, enabling the acquisition of high-resolution vertical SSC profiles(Liu et al., 2022). Inter-sensor consistency was verified before deployment, and turbidity (FTU) was calibrated to SSC using sediment samples from experiment location according to Guo et al.(2016), resulting in a robust linear relationship ($R^2 = 0.97$, Fig.3). Given the focus on tidal-scale morphodynamic trends, the raw bed-level time series were processed using a 5-minute average. This averaging suppresses transient signal fluctuations, providing a stabilized sequence for the calculation of bed level change.

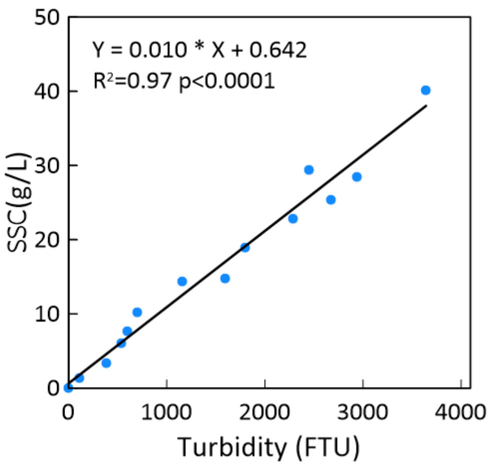

Figure 3: Calibration of the turbidity signal with SSC data.

https://doi.org/10.5194/egusphere-2026-5514
Preprint. Discussion started: 17 September 2026

4 Results

4.1 Hydrodynamics

The field experiments lasted for eight tidal cycles (defined as the period between two consecutive low tides, T1-T8; Fig. 4a). Despite the neap-to-spring transition, the tidal range was relatively stable, with the maximum water depth (h) at the site varied between 2.8 m and 3.2 m (Fig. 4a). Based on a significant wave height (H_s) threshold of 0.3 m, the tidal cycles were partitioned into storm(T1-T3) and fair-weather(T4-T8) periods.

Throughout the observation period, H_s increased sharply during the storm period, reaching a peak of approximately 1.1 m in T1(Fig. 4b). As the storm decayed, H_s decayed rapidly to below 0.3 m during the transition period and remained around 0.2 m during the calm phase, which is comparable to the local average summer wave height, and wave shoaling process became more prominent. The significant wave period T_s remained steady at approximately 8 s and increased to 12 s at the end of observation.

The wind and current velocities exhibited distinct temporal variations in response to the typhoon passage (Fig. 4c, d). During the initial phase of the storm (T1), the wind was predominantly directed toward the southwest with speeds ranging from 5 to 8 m s^{-1}. Coinciding with the typhoon landfall on July 28 (indicated by the black triangle), a sharp reversal in wind direction occurred, shifting abruptly to the north/northeast. This shift was accompanied by a peak wind velocity exceeding 12 m s^{-1}.

The nearshore currents showed a strong coherence with the wind forcing (Fig. 4d). During T1, the current flowed southeastward, reaching velocities of approximately 0.15 m s^{-1}. Following the shift in wind direction at T2, the current rapidly reversed its course, flowing northward/northwestward and attaining a maximum velocity of ~0.3 m s^{-1}. After the storm passed (T3–T8), both wind and current energies decayed significantly; wind speeds dropped below 5 m s^{-1}, and current velocities decreased to negligible (< 0.05 m s^{-1}), indicating the restoration of a calm, tide-dominated environment.

The evolution of total bed shear stress τ_{cw} directly reflects the extreme intensity of the typhoon (Fig. 5e). During the storm period, τ_{cw} reached a maximum of 6 N m^{-2}—significantly higher than the ~0.5 N m^{-2} seen during calm periods. Throughout the storm, wave-induced stress (τ_w) consistently dominated current-induced stress (τ_c), identifying wave orbital motion as the primary driver of bed forcing. However, alongshore currents raised the τ_{cw} to ~5 N m^{-2} during the transition period. In the calm period, both τ_c and τ_w remained below 1 N m^{-2}, τ_{cw} was close to or even below the τ_{cr} (~0.17 N m^{-2}) except low tide.

https://doi.org/10.5194/egusphere-2026-5514
Preprint. Discussion started: 17 September 2026

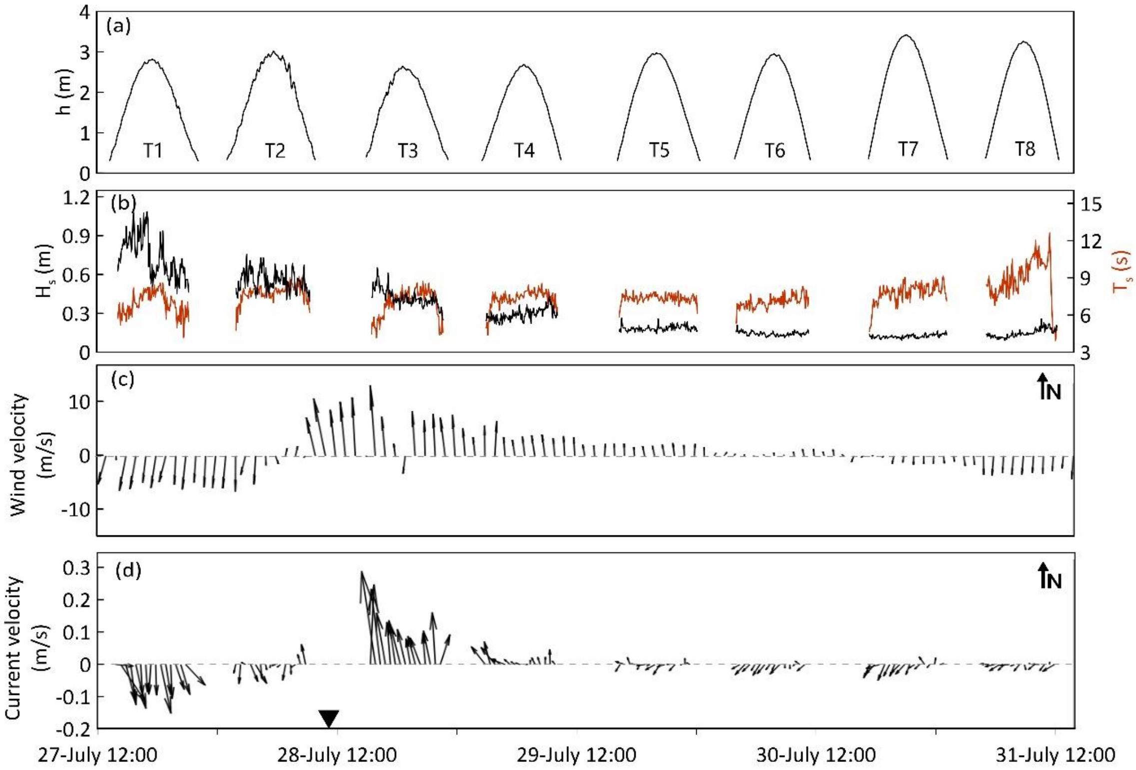

195 Figure 4: Time series of measured hydrodynamics parameters. (a) water depth (h); (b) significant wave height (H_s) and significant wave period ($\boldsymbol{T_s}$); (c) wind speed and direction; (d) current velocity (0.2mab) and direction; the black solid triangle indicates the time of typhoon landfall.

https://doi.org/10.5194/egusphere-2026-5514
Preprint. Discussion started: 17 September 2026

4.2 Suspended sediment concentration

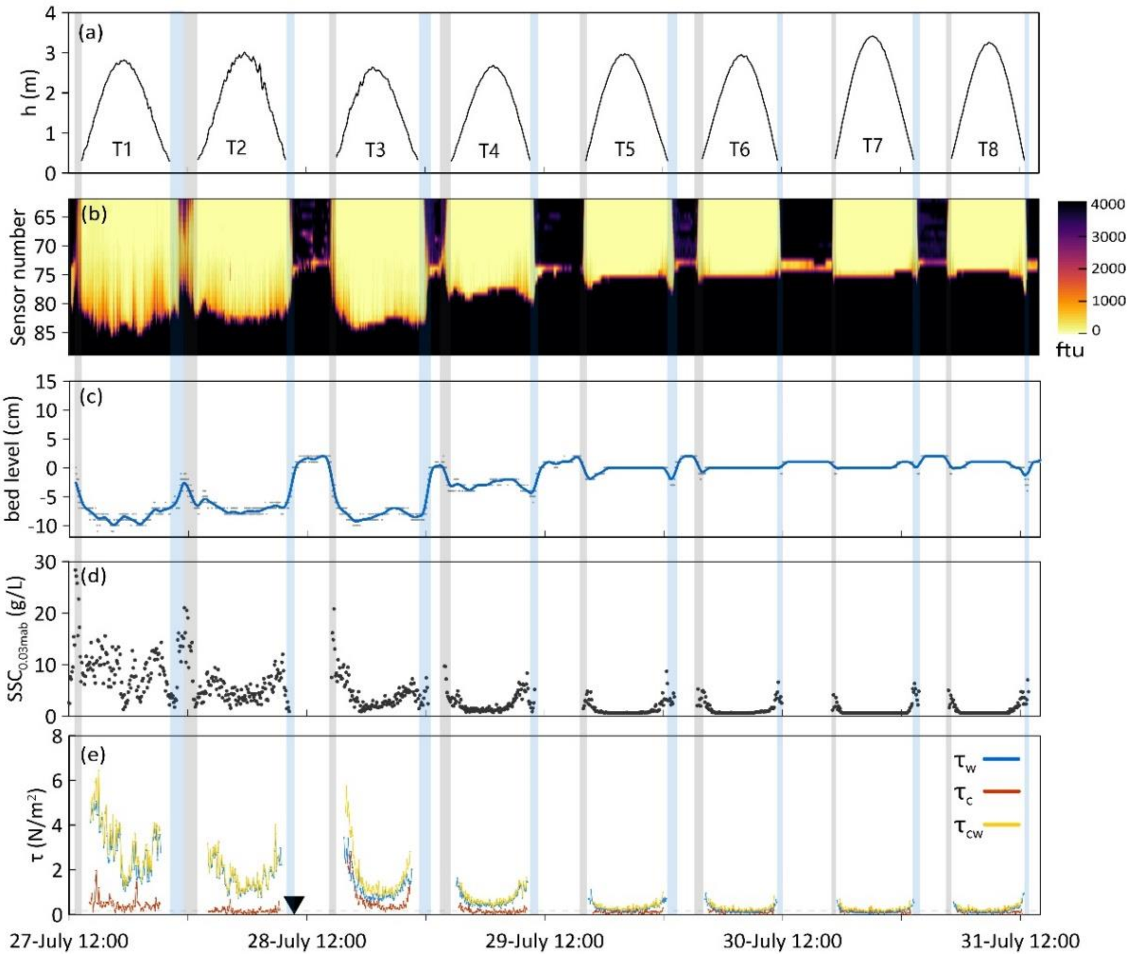

Figure 5: Time-series of (a) water depth (h); (b) vertical profiles of turbidity; (c)continuous bed level (gray dot)and its 1-hour moving average (blue line); (d) near-bed (0.3mab) suspended sediment concentration (SSC); (e) bed shear stress induced by wave (τ_w), current (τ_c) and combined wave and current (τ_{cw}), the dashed line indicates the critical shear stress (τ_{cr}). Gray and blue bars indicate ESWS in flood tide and ebb tide. The black solid triangle indicates the time of typhoon landfall.

The evolution of near-bed SSC is closely aligned with bed shear stress, SSC decreased from ~25 g L^{-1} during the storm period to 5 g L^{-1} during the calm period (Fig. 5 d). A strong positive linear correlation was found between SSC and τ_w (Fig. 6). However, this relationship exhibited a distinct asymmetry across different conditions: (1) the slope of the regression line under fair weather conditions was significantly higher than that during the storm period (Fig. 6a); (2) the slope of ebb tide (blue line) was significantly steeper than the flood tide (red line), indicating that for the same τ_w, a higher SSC was produced during the ebb tide (Fig. 6b).

https://doi.org/10.5194/egusphere-2026-5514
Preprint. Discussion started: 17 September 2026

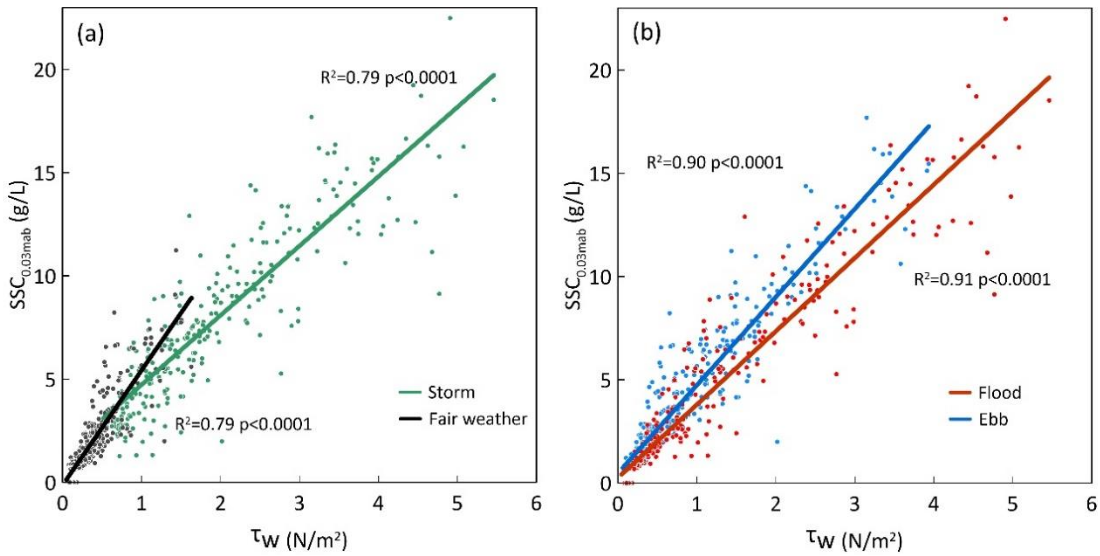

210 Figure 6: Correlation between wave-related bed shear stress (τ_w) and Suspended Sediment Concentration ($SSC_{0.03mab}$) categorized by (a) weather conditions (storm vs. fair weather) and (b) tidal phases (flood vs. ebb) during the RDWS.

4.3 Bed-Level Changes

4.3.1 Bed-Level Changes during flood and ebb

Results clearly revealed continuous bed-level changes during the storm process (Fig. 5c). They demonstrated that, despite the quasi-equilibrium observed at the tidal scale, the intra-tidal bed-level evolution showed a pronounced flood-ebb asymmetry (Fig. 7a). Regardless of energy conditions, the flood tide consistently caused bed erosion at the tidal-cycle scale, while the ebb tide consistently led to deposition.

During the storm period (T1–T3), the seabed was highly active, with the maximum bed-level erosion reaching -9.8 cm in T3. However, this erosion was substantially counterbalanced by considerable deposition in the following ebb phases—for example, accretion measured +8.0 cm during the ebb of T3 (Fig. 7a). As a result, despite marked intra-tidal fluctuations, the net bed-level change over complete tidal cycles stayed within a narrow band of 0–2 cm (Table 2), indicating a near dynamic equilibrium wherein ebb-phase deposition offsets flood-phase erosion.

During the fair-weather period (T4–T8), as wave energy diminishes, the magnitude of bed-level changes decreases significantly, the bed-level changes during both flood and ebb tides falls below 2 cm (Fig. 7a). Nevertheless, the distinct pattern of erosion on the flood tide and accretion on the ebb tide persists, confirming that this asymmetric morphology response is intrinsic to the intertidal zone, not merely an anomaly during storms.

https://doi.org/10.5194/egusphere-2026-5514
Preprint. Discussion started: 17 September 2026

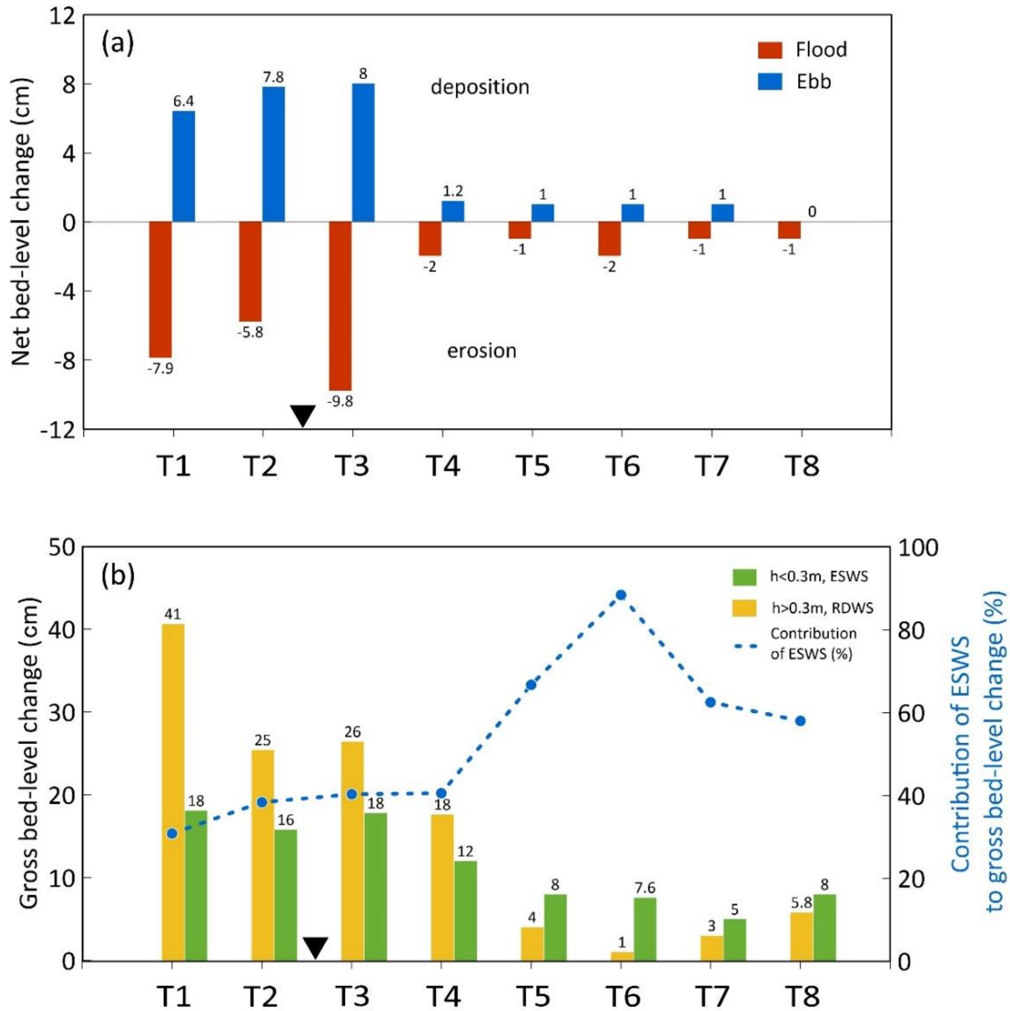

Figure 7: Bed-level changes across eight tidal cycles (T1–T8). (a) net bed-level changes (NBLC) occurring during flood (red) and ebb (blue) phases (positive: deposition; negative: erosion). The black triangle indicates the time of typhoon landfall. (b) gross bed-level change (GBLC) at water depths (h) of < 0.3 m (ESWS, green bar) and > 0.3 m (RDWS, yellow). The blue dashed line shows the ESWS contribution

4.3.2 Bed-Level Changes for Water Depths h < 0.3 m and h > 0.3 m

The gross bed-level change (GBLC) recorded during ESWS and RDWS reveals a distinct shift in morphodynamic dominance (Fig. 7b). During the storm period (T1–T3), RDWS dominated the gross bed-level change (GBLC). This was most evident in T1, where RDWS contributed 40.6 cm—roughly double the 18.1 cm recorded for ESWS (Table 2). However, in terms of gross rate, ESWS consistently exhibited higher dynamic intensity. Even in the RDWS-dominated T1, the change rate for ESWS (0.15 cm min^{-1}) was nearly twice that of RDWS (0.08 cm min^{-1}). As the storm weakened (T4–T8), the primary driver of bed

https://doi.org/10.5194/egusphere-2026-5514
Preprint. Discussion started: 17 September 2026

evolution shifted toward ESWS. By T6, ESWS contribution reached a peak of 88.4%, while the RDWS change dwindled to just 1.0 cm, with its rate falling to near-zero (<0.01 cm min^{-1}).

Overall, although the ESWS duration accounts for only 9.4%–19.5% of the tidal cycle (Table 2), it contributed more than 60% of the gross bed-level change from T5 to T8. This indicates that during fair weather, the intertidal morphology of dissipative beach is primarily driven by rapid hydrodynamic processes during the ESWS. In contrast, bed-level changes are controlled by deeper-water RDWS surf processes during storm event. Such a shift reveals distinct morphological response mechanisms between extreme events and recovery periods.

Table 2: Characteristics of net bed-level change (NBLC) and gross bed-level change (GBLC), including durations and change rates, during the ESWS and RDWS across tidal cycles T1–T8.

Tidal cycles				ESWS (Water Depths h < 0.3 m)					RDWS (Water Depths h > 0.3 m)					Ratio of ESWS to Tidal cycle	
	Duration (min)	NBLC (cm)	GBLC (cm)	Duration (min)	NBLC (cm)		GBLC (cm)	Rate (cm min^{-1})	Duration (min)	NBLC (cm)		GBLC (cm)	Rate (cm min^{-1})	Duration Ratio (%)	GBLC Ratio (%)
					Flood	Ebb				Flood	Ebb				
T1	660	-1.5	58.7	120	-5.9	5	18.1	0.15	540	-2	1.4	40.6	0.08	18.2	30.8
T2	665	2	41.2	130	-5.4	6.4	15.8	0.12	535	-0.4	1.4	25.4	0.05	19.5	38.4
T3	625	-1.8	44.2	115	-7	8.4	17.8	0.15	510	-2.8	-0.4	26.4	0.05	18.4	40.3
T4	595	-0.8	29.6	115	-3.6	4	12	0.10	480	1.6	-2.8	17.6	0.04	19.3	40.5
T5	575	0	12	75	-3	3	8	0.11	500	2	-2	4	0.01	13.0	66.7
T6	535	-1	8.6	75	-3	1	7.6	0.10	460	1	0	1	<0.01	14.0	88.4
T7	530	0	8	50	-2	1	5	0.10	480	1	0	3	0.01	9.4	62.5
T8	500	-1	13.8	50	-3	3.8	8	0.16	450	2	-3.8	5.8	0.01	10.0	58.0

5 Discussion

5.1 Role of storm events in intra-tidal Bed-level evolution

Results indicate that the overall intra-tidal bed-level changes generally followed a "flood erosion and ebb deposition" pattern (Fig. 7a), consistent with findings for tidal flats (Shi et al., 2019). This study, however, further reveals a divergence in intra-tidal mechanisms under different hydrodynamic conditions. While the ESWS maintained the "flood erosion and ebb deposition" pattern throughout the observations, the RDWS shifted to a "flood deposition and ebb erosion" pattern during the subsequent fair-weather period (Table 2). We attribute this shift to the storm's role in enhancing cross-shore sediment exchange and the varying bed shear stress during the RDWS.

During the storm period, RDWS morphodynamics were dominated by intense "flood erosion and ebb deposition." The significantly flatter slope of the τ_w–SSC regression compared to calm periods (Fig. 6a) indicates that the water column was undersaturated with sediment. Moreover, the higher SSC during ebb tides compared to flood tides under similar bed shear stress (Fig. 6b) suggests that sediment from an external source contributed to deposition during ebb. During the flood tide at RDWS, the high sediment transport capacity far exceeded the local sediment supply, driving continuous erosion (Fig. 8a).

https://doi.org/10.5194/egusphere-2026-5514
Preprint. Discussion started: 17 September 2026

During the subsequent ebb, as the surf zone migrated seaward, sediment-laden water was advected to the station. The resulting high local sediment concentration then exceeded the ebb tide transport capacity, leading to net deposition.

In contrast, during the fair-weather period, the RDWS pattern reversed to "flood deposition and ebb erosion." The steeper τ_w–SSC regression slope (Fig. 6a) reflects a more sensitive, supply-limited response to wave forcing. During the flood tide at RDWS, as τ_w approached or fell below the critical shear stress (τ_{cr}) for erosion (Fig. 5e), suspended sediment settled. Then the sediment easily resuspended during the subsequent ebb tide by increasing wave action, resulting in the observed ebb-phase erosion (Fig. 8b). This shift in intra-tidal mechanism underscores a fundamental transition in dissipative beach evolution, from a storm-dominated, "energy-driven" regime to a fair-weather, "supply-sensitive" regime.

https://doi.org/10.5194/egusphere-2026-5514
Preprint. Discussion started: 17 September 2026

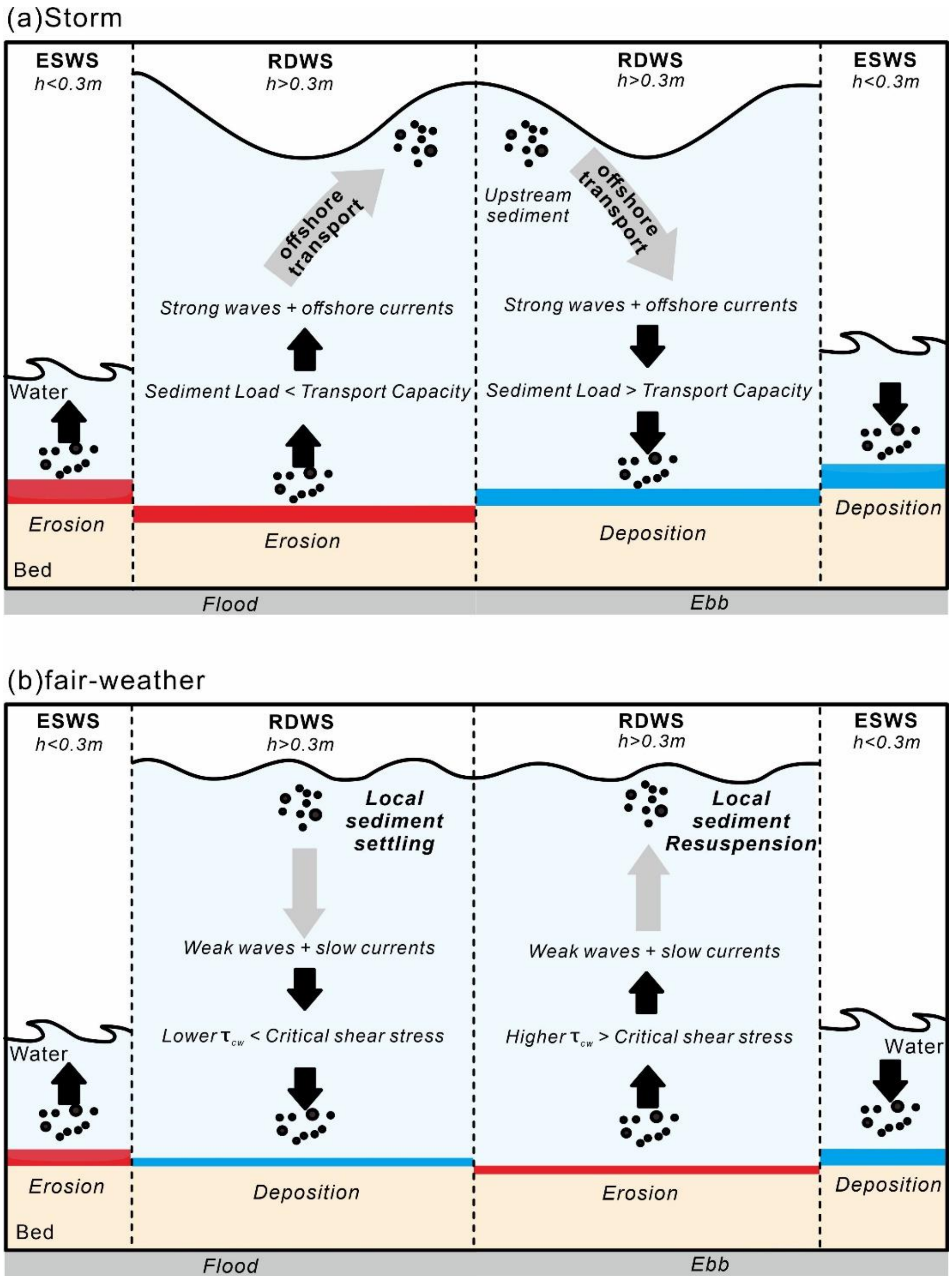

Figure 8: A conceptual model illustrating intertidal morphodynamics on a macrotidal beach under (a) storms, (b) fair-weather.

Notably, while a similar "flood erosion and ebb deposition" pattern has been reported on wave-dominated beaches (Berni et al., 2009; Hu et al., 2023), the underlying driving mechanisms are fundamentally different. In such settings, a high relative wave height (H/h) is typical, and water depth constrains incident wave height. Consequently, intertidal hydrodynamic forcing generally intensifies with rising tide levels (Aagaard et al., 2012; Li et al., 2022). By contrast, in our study, water depth significantly exceeds wave height. Therefore, incident wave height is less modulated by tidal fluctuation; instead, τ_w and wave-induced bed disturbance actually weaken as the water level increases (Fig. 5). These findings suggest that while wave energy dictates the magnitude of morphological change, macro-tides profoundly shape the evolution process by modulating the interaction between waves and the seabed. This highlights the complex influence of surf-zone migration and cross-shore sediment supply on the morphological evolution of macro-tidal intertidal zones.

5.2 Bed Level changes between Water Depths h < 0.3 m and h > 0.3 m

By quantitatively decomposing the distinct water-depth stages within each tidal cycle, this analysis reveals a shift in the dominant hydrodynamic mechanisms during the storm evolution. During the storm period, strong incident wave energy established the RDWS as the primary driver of morphological change. As shown in Table 2, the GBLC generated in the RDWS during T1 reached 40.6 cm, far exceeding the 18.1 cm recorded during the ESWS. Consequently, the RDWS dominated the GBLC in storm period (Fig. 7b), demonstrating that deep-water surf processes are the core mechanism for intertidal reshaping. However, the dominant driver of bed-level shifted as storm energy decayed. During fair-weather period, bed shear stress in the RDWS dropped rapidly toward τ_{cr} as rising tide, causing morphological activity to become negligible (Fig. 5e). During this period, wave breaking and surf processes were concentrated in shallow water, where sediment transport fluxes are notably higher than during the deeper wave-shoaling phase (Houwelingen et al., 2008; Ruessink et al., 2016). This change resulted in the ESWS producing greater bed-level changes relative to the RDWS (Fig. 7b). Specifically, the contribution of ESWS to GBLC rose from 30.8% in T1 to 88.4% in T6 (Table 2).

Additionally, research on tidal flats indicates that the NBLC induced by the ESWS are typically below 2 cm under windy conditions and less than 0.5 cm in calm weather (Shi et al., 2017, 2019). In contrast, the maximum NBLC observed during the ESWS on observed dissipative beach reached approximately 8 cm (storm) and 2 cm (calm)—roughly five times greater. This discrepancy is attributed to sediment characteristics, the muddy tidal flats have smaller pores and higher τ_{cr} compared to the sandy bed(Zhu et al., 2022). Therefore, even under comparable wind speeds (~13.6 m s^{-1}), muddy beds exhibit greater erosion resistance.

In summary, the RDWS dominates large-scale sediment transport under extreme hydrodynamics, while the ESWS maintains morphological stability after the tidal cycle through continuous and efficient transport, with bed sediment type acting as a critical factor in the degree of morphological change.

5.3 Implications and limitations

Storm events can reshape intertidal dynamics within a single tidal cycle, altering the role of the ESWS in bed-level evolution. Consequently, effective coastal management depends on a complete understanding of morphological processes, including those at the lowest water levels. Intertidal beach stability is inherently a tidal-scale dynamic equilibrium of the sediment budget. On dissipative beaches, low-water processes during flood tides generate landward flow and sediment transport, while ebb tides drive sediment seaward (Puleo et al., 2014), resulting in erosion of the lower intertidal zone during flood and deposition during

https://doi.org/10.5194/egusphere-2026-5514
Preprint. Discussion started: 17 September 2026

ebb (Duncan, 1964). Although this pattern is consistent with our observations throughout most tidal cycles, storm surges present a clear exception. Between T1 and T2, the observation station was not fully exposed and the topography did not recover to its pre-flood level (Fig. 5). This observation highlights the importance of the complete alternation of tidal processes for morphological stability. It suggests that when external forcing, such as storm surge, disrupts the full cycle of internal sediment dynamics, the self-adjustment capability of the beach system can be temporarily exceeded, resulting in net morphological change. Consequently, full ESWS duration is vital for stabilizing intertidal bed elevations.

A key limitation of this study is the absence of synchronized hydrodynamic measurements during the ESWS, which precluded a detailed discussion of the morphodynamic mechanisms in that stage. Future work should focus on three priorities: (1) deploying hydrodynamic sensors capable of operating in extremely shallow water; (2) considering that the proportion of the ESWS duration within a tidal cycle increases in the upper intertidal zone, morphological evolution at landward locations should be compared to determine its influence; and (3) since the sediment sources for dunes behind beaches are often debated (He et al., 2022; Walker et al., 2017), hydrodynamic-morphological observations during low-water exposure and submergence may be key to explaining dune development. Synchronized observations in both air and water are necessary to improve our understanding of the beach-dune system.

6 Conclusions

This study elucidates the intra-tidal bed-level dynamics of a dissipative macrotidal beach during storm attenuation. We demonstrate that storm attenuation not only reduces the overall magnitude of bed-level changes but also triggers a shift in the primary driver of morphological evolution from Relatively Deep Water Stages (RDWS) to Extremely Shallow Water Stages (ESWS). The main conclusions are as follows:

Shifts in intra-tidal patterns: Under storm forcing, the RDWS exhibits intense "flood erosion and ebb deposition". As wave energy decays, this pattern reverses to "flood deposition and ebb erosion," highlighting a fundamental transition from energy-driven to tide-modulated dynamics. In contrast, the ESWS maintains a more stable evolution pattern across different energy levels due to its continuous and efficient sediment transport processes.

Switching of dominant processes: During the storm period, the RDWS contributes rapid intertidal reshaping, with gross bed-level change reaching 40.6 cm. Under fair-weather conditions, as RDWS dynamics subsided, the ESWS maintained relatively high bed-level change rates, increasing its contribution to total GBLC from 30.8% in T1 to a maximum of 88.4% in T6. Furthermore, the maximum bed-level change observed in the ESWS (~8 cm) is significantly greater than those recorded on tidal flats, revealing critical differences in erosion resistance between sandy and muddy beds.

Implications for management: The stability of the dissipative beach depends on the integrity of the complete tidal cycle. Disruptions to low-water ESWS processes (e.g., by storm surges) can break the sediment budget balance, leading to morphological changes. Therefore, future coastal management must incorporate these extreme shallow-water processes.

Data availability

Data available at https://doi.org/10.5281/zenodo.22707706.

Author contributions

ZX and FC conceived the study and designed the field campaign. ZX performed the data processing and analysis, prepared the figures, and wrote the original draft. FC supervised the study and contributed to the interpretation of the results and manuscript revision. SZ, GL, YH, CC, CW, HY, and BH contributed to the field investigation and data collection. HQ, BS, and SZ contributed to the interpretation of the hydrodynamic and sediment-transport processes. FC contributed to funding acquisition and project administration. All authors reviewed and approved the final manuscript.

Competing interests

The authors declare no competing interests.

Acknowledgements

We thank John R. C. Hsu for the valuable suggestions in revising the manuscript, and Shasha Liu, Yi Sun, Kai Liu, Weile Zheng for their assistance during the fieldwork.

Financial support

This work has been funded by the National Natural Science Foundation of China (No. U22A20585, No 42206171), the Natural Science Foundation of Fujian Province, China (No. 2023J05071, No. 2023J0113712, No. 2024J08100), and the Scientific Research Foundation of the Third Institute of Oceanography, Ministry of Natural Resources (No. 2023011, No. 2024019).

References

Aagaard, T., Hughes, M. G., Baldock, T. E., Greenwood, B., Kroon, A., and Power, H. E.: Sediment transport processes and morphodynamics on a reflective beach under storm and non-storm conditions, Marine Geology, 326, 154–165, https://doi.org/10.1016/j.margeo.2012.09.004, 2012.

Aagaard, T., Greenwood, B., and Hughes, M.: Sediment transport on dissipative, intermediate and reflective beaches, Earth-Science Reviews, 124, 32–50, https://doi.org/10.1016/j.earscirev.2013.05.002, 2013.

Aagaard, T., Hughes, M. G., and Ruessink, G.: Field Observations of Turbulence, Sand Suspension, and Cross-Shore Transport Under Spilling and Plunging Breakers, JGR Earth Surface, 123, 2844–2862, https://doi.org/10.1029/2018JF004636, 2018.

Anthony, E. J. and Aagaard, T.: The lower shoreface: Morphodynamics and sediment connectivity with the upper shoreface and beach, Earth-Science Reviews, 210, 103334, https://doi.org/10.1016/j.earscirev.2020.103334, 2020.

António, S. D., Werf, J. van der, Horstman, E., Cáceres, I., Alsina, J., Zanden, J. van der, and Hulscher, S.: Influence of Beach Slope on Morphological Changes and Sediment Transport under Irregular Waves, Journal of Marine Science and Engineering, 11, https://doi.org/10.3390/jmse11122244, 2023.

Berni, C., Mignot, E., Michallet, H., Dalla-Costa, C., Grasso, F., and Lagauzre, M.: Diversity of bed evolution at wave and tidal scales on Truc-Vert beach, Journal of Coastal Research, 1726–1730, 2009.

Blenkinsopp, C. E., Turner, I. L., Masselink, G., and Russell, P. E.: Swash zone sediment fluxes: Field observations, Coastal Engineering, 58, 28–44, https://doi.org/10.1016/j.coastaleng.2010.08.002, 2011.

Brand, E., Chen, M., and Montreuil, A. L.: Optimizing measurements of sediment transport in the intertidal zone, Earth-Sci. Rev., 200, 10, https://doi.org/10.1016/j.earscirev.2019.103029, 2020.

Duncan, J. R.: The effects of water table and tide cycle on swash-backwash sediment distribution and beach profile development, Marine Geology, 2, 186–197, https://doi.org/10.1016/0025-3227(64)90039-8, 1964.

Fan, Z., Zhu, X., Xu, H., Sun, Z., Zhang, H., Bi, X., Hu, C., Lu, D., Sun, Z., Li, K., Quan, Y., and Jia, Y.: A new method for long-term in situ monitoring of seabed interface evolution: A self-potential probe, Ocean Engineering, 280, 114917, https://doi.org/10.1016/j.oceaneng.2023.114917, 2023.

Gilpin, M.: A snapshot of suspended sediment concentrations and fluxes using optical and acoustic velocity profilers, the Stour Estuary, Suffolk, UK, ARGUS GESELLSCHAFT FUER UMWELTMESSTECHNIK MBH, 2003.

Grant, W. D. and Madsen, O. S.: Combined wave and current interaction with a rough bottom, J. Geophys. Res., 84(C4), 1797–1808, https://doi.org/10.1029/JC084iC04p01797, 1979.

Grasso, F., Michallet, H., Barthélemy, E., and Certain, R.: Physical modeling of intermediate cross-shore beach morphology: Transients and equilibrium states, Journal of Geophysical Research: Oceans, 114, https://doi.org/10.1029/2009JC005308, 2009.

Guo, L., Wen, M., Shan, H., Liu, X., Zhang, S., Wang, Z., and Jia, Y.: Study on re-suspension process of seabed sediment induced by wave., Marine Geology & Quaternary Geology (in Chinese), 181–188, 2016.

He, Y., Liu, J., Cai, F., Li, B., Qi, H., and Zhao, S.: Aeolian sand transport influenced by tide and beachface morphology, Geomorphology, 396, https://doi.org/10.1016/j.geomorph.2021.107987, 2022.

Houwelingen, S. van, Masselink, G., and Bullard, J.: Dynamics of multiple intertidal bars over semi-diurnal and lunar tidal cycles, North Lincolnshire, England, Earth Surface Processes and Landforms, 33, 1473–1490, https://doi.org/10.1002/esp.1616, 2008.

Hu, P., Li, Z., Zeng, C., Zhu, D., Liu, R., Su, Q., Tang, J., and Zhu, Y.: Bed level changes in the surf zone during post-storm beach recovery, Front. Mar. Sci., 10, 1233068, https://doi.org/10.3389/fmars.2023.1233068, 2023.

Hu, Z., Lenting, W., van der Wal, D., and Bouma, T. J.: Continuous monitoring bed-level dynamics on an intertidal flat: Introducing novel, stand-alone high-resolution SED-sensors, Geomorphology, 245, 223–230, https://doi.org/10.1016/j.geomorph.2015.05.027, 2015.

Li, Y., Zhang, C., Song, J., Chi, S., Zhao, S., Qi, H., and Shi, J.: Tide-modulated wave characteristics and breaking regimes in the intertidal zone of a dissipative beach, Ocean Engineering, 266, 113055, https://doi.org/10.1016/j.oceaneng.2022.113055, 2022.

Liu, X., Ma, L., Zhang, H., Lu, Y., Chen, A., and Zhang, S.: Comparative Study of In-Situ Observation of Dynamics of Fluid Mud Layers on the Seafloor with Acoustic and Optical Instruments, PERIODICAL OF OCEAN UNIVERSITY OF CHINA (in Chinese), 51, 2021.

Liu, X., Lu, Y., Yu, H., Ma, L., Li, X., Li, W., Zhang, H., and Bian, C.: In-Situ Observation of Storm-Induced Wave-Supported Fluid Mud Occurrence in the Subaqueous Yellow River Delta, Journal of Geophysical Research: Oceans, 127, e2021JC018190, https://doi.org/10.1029/2021JC018190, 2022.

Masselink, G. and Puleo, J. A.: Swash-zone morphodynamics, Continental Shelf Research, 26, 661–680, https://doi.org/10.1016/j.csr.2006.01.015, 2006.

Masselink, G., Austin, M. J., O'Hare, T. J., and Russell, P. E.: Geometry and dynamics of wave ripples in the nearshore zone of a coarse sandy beach, Journal of Geophysical Research: Oceans, 112, https://doi.org/10.1029/2006JC003839, 2007.

Nielsen, P.: Coastal bottom boundary layers and sediment transport, World scientific, 1992.

Niu, J., Xie, J., Lin, S., Lin, P., Gao, F., Zhang, J., and Cai, S.: Importance of Bed Liquefaction-Induced Erosion During the Winter Wind Storm in the Yellow River Delta, China, Journal of Geophysical Research: Oceans, 128, e2022JC019256, https://doi.org/10.1029/2022JC019256, 2023.

Puleo, J. A.: Tidal Variability of Swash-Zone Sediment Suspension and Transport, Journal of Coastal Research, 254, 937–948, https://doi.org/10.2112/08-1031.1, 2009.

Puleo, J. A., Lanckriet, T., and Blenkinsopp, C.: Bed level fluctuations in the inner surf and swash zone of a dissipative beach, Marine Geology, 349, 99–112, https://doi.org/10.1016/j.margeo.2014.01.006, 2014.

Qi, H., Cai, F., Lei, G., Cao, H., and Shi, F.: The response of three main beach types to tropical storms in South China, Marine Geology, 275, 244–254, https://doi.org/10.1016/j.margeo.2010.06.005, 2010.

Rangel-Buitrago, N. and Anfuso, G.: Coastal storm characterization and morphological impacts on sandy coasts, Earth Surface Processes and Landforms, 36, 1997–2010, https://doi.org/10.1002/esp.2221, 2011.

Ruessink, B. G., Blenkinsopp, C., Brinkkemper, J. A., Castelle, B., Dubarbier, B., Grasso, F., Puleo, J. A., and Lanckriet, T.: Sandbar and beach-face evolution on a prototype coarse sandy barrier, Coastal Engineering, 113, 19–32, https://doi.org/10.1016/j.coastaleng.2015.11.005, 2016.

Shi, B., Cooper, J. R., Pratolongo, P. D., Gao, S., Bouma, T. J., Li, G., Li, C., Yang, S. l., and Wang, Y. P.: Erosion and Accretion on a Mudflat: The Importance of Very Shallow-Water Effects, Journal of Geophysical Research: Oceans, 122, 9476–9499, https://doi.org/10.1002/2016JC012316, 2017.

Shi, B., Cooper, J. R., Li, J., Yang, Y., Yang, S. L., Luo, F., Yu, Z., and Wang, Y. P.: Hydrodynamics, erosion and accretion of intertidal mudflats in extremely shallow waters, Journal of Hydrology, 573, 31–39, https://doi.org/10.1016/j.jhydrol.2019.03.065, 2019.

Soulsby, R.: Dynamics of Marine Sands: A Manual for Practical Applications, Thomas Telford, London, 1997..

https://doi.org/10.5194/egusphere-2026-5514
Preprint. Discussion started: 17 September 2026

Swart, D. H.: Offshore sediment transport and equilibrium beach profiles, Delft Hydraulics, Pub., 131, 1974.

Turner, I. L. and Masselink, G.: Swash infiltration-exfiltration and sediment transport, Journal of Geophysical Research: Oceans, 103, 30813–30824, https://doi.org/10.1029/98JC02606, 1998.

Walker, I. J., Davidson-Arnott, R. G. D., Bauer, B. O., Hesp, P. A., Delgado-Fernandez, I., Ollerhead, J., and Smyth, T. A. G.: Scale-dependent perspectives on the geomorphology and evolution of beach-dune systems, Earth-Science Reviews, 171, 220–253, https://doi.org/10.1016/j.earscirev.2017.04.011, 2017.

Wen, M., Jia, Y., Wang, Z., Zhang, S., and Shan, H.: Wave flume experiments on dynamics of the bottom boundary layer in silty seabed, Acta Oceanol. Sin., 39, 96–104, https://doi.org/10.1007/s13131-020-1571-7, 2020.

van der Werf, J. J., Schrijvershof, R. A., Brakenhoff, L. B., and Grasmeijer, B. T.: Observations of near-bed orbital velocities and small-scale bedforms on the Dutch lower shoreface, Ocean & Coastal Management, 218, 106012, https://doi.org/10.1016/j.ocecoaman.2021.106012, 2022.

Wright, L. D. and Short, A. D.: Morphodynamic variability of surf zones and beaches: A synthesis, Marine Geology, 56, 93–118, https://doi.org/10.1016/0025-3227(84)90008-2, 1984.

Zhang, Q., Gong, Z., Zhang, C., Zhou, Z., and Townend, I.: Hydraulic and Sediment Dynamics at times of Very Shallow Water on Intertidal Mudflats: The Contribution of Waves, Journal of Coastal Research, 75, 507–511, https://doi.org/10.2112/SI75-102.1, 2016.

Zhu, S., Chen, Y., Yan, W., Xing, F., Li, R., Li, M., Shi, B., and Wang, Y. P.: The Hummocky Patches and Associated Sediment Dynamics Over an Accretional Intertidal Flat, Front. Earth Sci., 10, https://doi.org/10.3389/feart.2022.908351, 2022.